The Cryosphere Discuss., 7, 4207–4240, 2013
www.the-cryosphere-discuss.net/7/4207/2013/
doi:10.5194/tcd-7-4207-2013

The Cryosphere Discussions
Open Access

Frontal ablation and temporal variations in surface velocity of Livingston Island ice cap, Antarctica

B. Osmanoglu[1], M. I. Corcuera[2], F. J. Navarro[2], M. Braun[3], and R. Hock[1]

[1]Geophysical Institute, University of Alaska Fairbanks, P.O. Box 757320 Fairbanks, Alaska 99775, USA
[2]Dept. Matemática Aplicada, ETSI de Telecomunicación, Universidad Politécnica de Madrid, Av. Complutense, 30, 28040 Madrid, Spain
[3]Institute of Geography, University of Erlangen, Kochstrasse 4/4, 91054 Erlangen, Germany

Received: 30 June 2013 – Accepted: 15 July 2013 – Published: 26 August 2013

Correspondence to: B. Osmanoglu (batu@gi.alaska.edu)

Published by Copernicus Publications on behalf of the European Geosciences Union.

Abstract

Frontal ablation from marine-terminating glaciers and ice caps covering the islands off the western coast of the Antarctic Peninsula is poorly known. Here we estimate the frontal ablation from the ice cap of Livingston Island, the second largest island in the South Shetland Islands archipelago, using glacier surface velocities obtained from intensity offset tracking of PALSAR-1 imagery and glacier ice thickness inferred from principles of glacier dynamics and calibrated against ground-penetrating radar (GPR) measurements of ice thickness. Using 21 SAR images acquired between October 2007 and January 2011, we obtain surface velocities of up to 250 m yr^{-1} and an average frontal ablation rate of about 509 ± 381 Mt yr^{-1}, equivalent to a specific mass change of -0.7 ± 0.5 m w.e. yr^{-1} over the area of the ice cap (697 km^2). A rough estimate of the surface mass balance of the ice cap gives 0.1 ± 0.1 m w.e. yr^{-1}, resulting in a total mass balance for Livingston Island ice cap of -0.6 ± 0.5 m w.e. yr^{-1}. We find that frontal ablation and surface ablation contribute equal shares to total ablation. We also find large changes in frontal ablation rate (of ~ 237 Mt yr^{-1}) due to temporal variability in surface velocities. This highlights the importance of taking into account the seasonality in ice velocities when computing frontal ablation with a flux-gate approach.

1 Introduction

More than 99 % of the glacierized area of the islands in the periphery of the Antarctic Peninsula drains through marine termini or into ice shelves (Bliss et al., 2013), but little is known about the magnitude and relative importance of mass loss through frontal ablation (i.e. the sum of iceberg calving and submarine melting) at these termini. A few studies on marine-terminating ice caps in the Arctic show that frontal ablation might account for roughly 30–40% of the total ablation (Dowdeswell et al., 2002, 2008). Shepherd et al. (2012) give an estimate of mass loss (1992–2011) for the entire Antarctic Peninsula of -20 ± 14 Gt yr^{-1} excluding glaciers and ice caps of the Antarctic periphery.

TCD
7, 4207–4240, 2013

Since assessing and modelling of calving (Benn et al., 2007b, a; Amundson and Truffer, 2010; Otero et al., 2010; Bassis, 2011; Vieli and Nick, 2011) and submarine melt (Motyka et al., 2003; Enderlin and Howat, 2013) are inherently difficult, mass changes by frontal ablation are often neglected or under-represented in regional and global-scale mass budget assessments and projections (Radić and Hock, 2011; Cogley, 2012; Marzeion et al., 2012; Giesen and Oerlemans, 2013; Radić et al., 2013) leading to systematic underestimation of mass loss. While mass loss through surface melting is reasonably well understood, the processes involved in frontal ablation are largely non-linear and operate on time scales that are not necessarily linked to regional climate variations (Truffer and Fahnestock, 2007). There is a need to better quantify the dynamic mass losses because they provide a mechanism for glaciers to lose mass much more rapidly than is possible through other means.

For the glaciers and ice caps covering the islands off the western coast of the Antarctic Peninsula, some estimates of frontal ablation have appeared recently (Osmanoglu et al., 2013a; Navarro et al., 2013). Such estimates are crucial to understand the evolution of the mass balance in a region that has shown considerable regional warming (Steig and Orsi, 2013; Turner et al., 2013).

Here we estimate the average frontal ablation rate of the ice cap on Livingston Island, the second largest island in the South Shetland Islands archipelago, located northwest of the tip of the Antarctic Peninsula (Fig. 1), for the period October 2007–January 2011. By frontal ablation we mean the loss of mass from the near-vertical calving fronts of the marine-terminating glaciers, including losses by calving, subaqueous melting, and subaerial melting and sublimation (Cogley et al., 2011). We adopt a flux-gate method approximating frontal ablation by the ice discharge through defined flux-gates close to the marine termini. Hence, the approach does not distinguish between the individual components of frontal ablation. It requires the knowledge of both ice velocities and ice thickness at given flux gates. Radar remote sensing data are used to derive ice velocities, which in turn are used to approximate ice thicknesses based on principles of glacier dynamics and calibrated against the available GPR-retrieved ice thickness.

TCD
7, 4207–4240, 2013

We also investigate the temporal variations of ice velocity, and their seasonality, at the defined flux gates. For our analyses we compile a new 50 m × 50 m resolution DEM by merging existing data sets with satellite-derived elevations.

2 Study area

Livingston Island ice cap (62°28′–62°45′ S, 59°49′–60°59′ W) is about 60 km long and 30 km wide. The glacier-covered area was 734 km^2 in 1956 and shrunk by 4.3 % during the period 1956–1996, to a glacierized area of 703 km^2 in 1996 (Calvet et al., 1999). Our latest estimate using the 2004 outlines (unpublished data from Jaume Calvet and David García-Sellés) is 697 km^2. Glaciological field campaigns have been conducted in recent years on several glaciers of the ice cap. A 10 yr surface mass balance record is available for Hurd and Johnsons Glaciers, indicating a nearly balanced mass budget over the observation period 2002–2011 (Navarro et al., 2013) and a deceleration of losses from these glaciers from 1957–2000 to 2002–2011. Jonsell et al. (2012) applied a distributed temperature-radiation index melt model calibrated against automatic weather station and in-situ surface mass balance data from Hurd Peninsula glaciers revealing a high sensitivity of the mass balance of the ice cap to climate change. They showed that a 0.5 °C temperature increase results in 56 % higher melt rates, which is mainly an effect of the on-glacier summer average temperatures being close to zero. In-situ ice velocity measurements are available on Hurd Peninsula (Ximenis et al., 1999; Otero, 2008; Otero et al., 2010), and ice thickness retrieved from GPR measurements are limited to certain locations on the island (see details in Sect. 3). A summary of other previous glaciological studies on the island and the Antarctic Peninsula region can be found in Navarro et al. (2013).

TCD
7, 4207–4240, 2013

3 Data

3.1 Ice thickness

Ice thickness data are only available for limited parts of the ice cap. These were retrieved from 20 MHz ground-based GPR measurements carried out in December 2000 along the main ice divides of the western part of the island and, in December 2006, on Bowles Plateau (BP in Fig. 2), which is the accumulation area of Perunika Glacier (21 in Fig. 2). The data are described in Macheret et al. (2009). Typical thickness under the western divides is ~ 150 m, reaching maxima of ~ 200 m, and the average thickness under Bowles Plateau is ~ 265 m, with maximum thicknesses of 500 m. GPR measurements on Hurd Peninsula glaciers carried out at different radar frequencies and various dates are described in Navarro et al. (2009), and show an average thickness of ~ 94 m and maximum values of ~ 200 m.

3.2 In situ surface velocities

In situ glacier surface velocity measurements in Livingston Island are only available on Hurd Peninsula (Ximenis et al., 1999; Otero, 2008; Otero et al., 2010). Johnsons Glacier, a tidewater glacier, has velocities increasing from zero at the ice divides to typical year-averaged values close to $40\,\mathrm{m\,yr^{-1}}$ in the fastest part of its calving front. But, for most of its area, the velocities are below $10\,\mathrm{m\,yr^{-1}}$. Hurd Glacier, which terminates on land, has lower velocities, with observed year-averaged values always below $5\,\mathrm{m\,yr^{-1}}$. The maximum velocities are observed in the upper ablation area, and strongly decrease near the glacier snout, which has been suggested to be frozen to bed based on geomorphological analyses and GPR studies (Molina et al., 2007; Navarro et al., 2009).

TCD
7, 4207–4240, 2013

3.3 SAR imagery

Synthetic Aperture Radar (SAR) data were used to derive surface ice velocities and to compile a new DEM for the ice cap. Data from two sources were included: (1) the PALSAR imaging system on board the Japanese Advanced Land Observing Satellite (ALOS-1) satellite and (2) Bistatic TanDEM-X pair from the TerraSAR-X and TanDEM-X satellites.

PALSAR-1 provides L-band (1270 MHz) signals and was operational during 2006–2011. We used two parallel tracks (124 and 125) covering the entire ice cap, which provided a total of 21 images between October 2007 and January 2011. All images were collected in Fine Beam Single Polarization mode, which gives a ground resolution of about 9 m×5 m. The images have a swath width of ∼ 70 km in the range direction.

The bistatic TanDEM-X pair was acquired by TerraSAR-X and TanDEM-X satellites simultaneously, generating high quality interferometric data by removing the effects of temporal decorrelation. These images have a ground resolution of about 3 m × 3 m and cover an area of about 30 km × 30 km. The X-band (9.65 GHz) signal penetrates very little into the snow and ice, the penetration depth depending on surface conditions. It hence enables the generation of accurate surface elevation models. Details on the exact penetration depth of the SAR signal are unknown. However, X-band penetration is generally considered to have maximum penetration depths of ∼ 10 m in dry snow, and less during wet snow conditions. The TanDEM-X acquisition occurred on 18 March 2012, at the transition from late summer to cooler winter conditions.

3.4 Digital elevation model

The only topographic maps available covering the entire Livingston Island are the 1 : 200 000 map by DOS (1968), based on aerial photos taken in 1957, and the 1 : 100 000 map by SGE (1997), based on SPOT images of 1991 and 1996.

TCD
7, 4207–4240, 2013

Since elevation is a crucial variable for our approach of calculating ice velocities, and an accurate high-resolution DEM is not available, we have compiled a new digital elevation model for Livingston Island with 50 m × 50 m grid cells (Fig. 3) based on:

1. the Radarsat Antarctic Mapping Project (RAMP) DEM (Liu, 2001),
2. radargrammetry using PALSAR-1 data,
3. Tandem-X bistatic interferometry,
4. the Advanced Spaceborne Thermal Emission and Reflection Radiometer (ASTER) Global DEM v.2,
5. the Ice, Cloud and Land Elevation Satellite (ICESat) elevation profiles, level 1B Global Elevation Data (GLA06) obtained from the National Snow and Ice Data Center (NSIDC).

The RAMP DEM covers the entire island with 200 m × 200 m grid cell resolution, which we resample to 50 m × 50 m (Fig. 3a). First, the RAMP DEM was sharpened using a SAR intensity image. The intensities of a SAR interferogram generated from PALSAR-1 images were used to estimate local slopes (Eineder, 2003). These were then scaled to the range between 0.75 and 1.25, and multiplied by the RAMP DEM to superimpose the obtained structure from the intensity image to the RAMP DEM, without altering the histogram of original elevation values (Fig. 3b). Even though the sharpened RAMP DEM has smaller scale variability, statistically its misfit to ICESat elevations did not change after this operation. For comparison, the ICESat laser footprint is ~ 60 m, separated by ~ 170 m along the ground track (Fig. 3c).

Second, additional higher-quality partial DEMs for the ice cap were generated. Radargrammetry was used to derive a ~ 160 m resolution DEM for the eastern half of the ice cap using PALSAR-1 data from two parallel tracks (Fig. 3d). PALSAR-1 data provided the two different look angles necessary for radargrammetry, while the relatively short 16 day baseline limited the amount of surface change due to glacier motion

TCD
7, 4207–4240, 2013

and snow cover between the two images (Balz et al., 2009). In addition, a higher resolution (10 m) DEM was generated from bistatic TanDEM-X interferometry (Fig. 3f). The unwrapping was done using a modified version of the SNAPHU unwrapping software, capable of multigrid unwrapping (Chen and Zebker, 2001). The entire InSAR processing was done at full resolution, though the final DEM was put on a 10 m × 10 m grid to increase redundancy and reduce gaps due to radar shadows. The DEM is restricted to the parts in the north-east of the ice cap that are covered by the satellite scene. We further used the 30 m resolution ASTER GDEM v.2 data, but the data are heavily affected by cloud cover. To ensure sufficient quality we only included pixels with three or more available observations, which reduced the coverage mostly to the south-eastern part of the ice cap (Fig. 3e).

A first order polynomial plane was removed from all digital elevation models and all were best-fitted to the ICESat data, finally getting resampled to 50 m pixel spacing before merging. The final elevation z for each pixel was obtained by taking weighted averages of the available data. The weights were selected adaptively as a function of the expected error and number of neighboring points:

$$z = \frac{\sum_{i=1}^{5} w_{\sigma}^{i} w_{\mathrm{n}}^{i} z^{i}}{\sum_{i=1}^{5} w_{\sigma}^{i} w_{\mathrm{n}}^{i}} \quad (1)$$

where i denotes five different data sets (sharpened RAMP, ICESat, radargrammetry, ASTER and TanDEM-X), w_{σ} denotes weighting based on expected error, and w_{n} is weighting based on the distance to the nearest neighbour. The expected RMSE for ASTER GDEM changes based on topography and number of observations available, ranging from 3 to 50 m (Reuter et al., 2009; Hirt et al., 2010; Hengl and Reuter, 2011). The TanDEM-X DEM is expected to provide 10 m absolute and 2–4 m relative vertical accuracy (Gonzalez et al., 2010). ICESat altimeter data is accurate to ∼ 0.3 m in vertical (Magruder et al., 2007). Accuracy of radargrammetry changes with topography, accuracy of correlation and orbit accuracy, and is expected to be on the order of 10–50 m (Balik et al., 2004; Balz et al., 2009, 2013). The RAMP DEM has spatially varying

TCD
7, 4207–4240, 2013

error, which increases with surface slope and is expected to be accurate to 30 m in vertical (Bamber and Gomez-Dans, 2005). The RMSE for the different DEMs compared with ICESat were 125, 146, 200, and 368 m for TanDEM-X, sharpened RAMP, radargrammetry and ASTER GDEM, respectively. The calculated deviations not only reflect differences in elevation between data sets but also the correlation between number of samples available for each data set. There were 259, 792, 200 and 51 points available for comparisons between ICESat and the other four DEMs (TanDEM-X, sharpened RAMP, radargrammetry and ASTER GDEM, respectively). For this analysis we gave equal weighting to ICESat and TanDEM-X DEM (std ~ 5 m), as well as ASTER GDEM and RAMP (std ~ 25 m). The radargrammetry had the lowest weight (std ~ 50 m). The combined DEM is shown in Fig. 3g and the standard deviation of errors relative to 792 ICESat measurements was 121 m.

4 Methods

4.1 Flux gates

In this study frontal ablation is approximated by the ice flux perpendicular to a theoretical surface across the glacier terminus called "flux gate". For robust estimation of the ice discharge across each flux gate, ten parallel flux gates at intervals of ~ 50 m were defined with the lowest gate as close as possible to the glacier termini, between roughly 100 and 600 m upglacier from the calving front. Ice discharges for all ten flux gates were calculated individually and averaged to obtain a mean value. Deviation of each flux gate from the mean was calculated and flux gates with deviations higher than 20 % of the mean were discarded. On average 7.5 flux gates were used for the analysis. Flux gates are only defined for marine terminating glaciers where the ice velocities at the flux gates exceed 20 m yr^{-1}. For the remaining tidewater and all land terminating glaciers ice discharge into the ocean is assumed negligible.

TCD
7, 4207–4240, 2013

4.2 Frontal ablation

For each marine-terminating glacier we compute the ice flux q across the corresponding flux gate. Following Rignot (1996) and Osmanoglu et al. (2013a), we derive the ice flux from surface velocities by

$$q = H\gamma u_{\mathrm{sfc}} \tag{2}$$

where H is ice thickness and γ is the ratio between thickness-averaged and surface u_{sfc} horizontal velocities for each grid cell. We assume $\gamma = 0.9$ (Cuffey and Paterson, 2010). u_{sfc} and H are a function of position along the flux-gate. The ice discharge D is then defined as the integral of ice flux perpendicular to the flux-gate over the length L of the flux gate:

$$D = \int_0^L q\rho_{\mathrm{ice}}\,\mathrm{d}l \tag{3}$$

where ρ_{ice} is the density of ice (900 kgm^{-3}). Flow directions are computed from offset tracking. Frontal ablation is given in units of $\mathrm{Mt\,yr}^{-1}$ throughout the paper.

4.3 Surface velocities

Intensity offset tracking method was used to obtain glacier surface velocities from PALSAR-1 intensity images (Gray et al., 1998; Strozzi et al., 2002; Werner et al., 2005; Strozzi et al., 2008). We preferred intensity offset tracking, rather than coherence tracking, because of the large extent of incoherent areas in the available imagery (Strozzi et al., 2002). In this study, inconsistent velocity measurements were masked out using a spatial variance filter, such that surface velocity measurements that have Fisher's Distance of $80\,\mathrm{m\,yr}^{-1}$ (with a constant expected error of $4\,\mathrm{m\,yr}^{-1}$) or above compared to their neighbors are discarded (Osmanoglu et al., 2011).

TCD
7, 4207–4240, 2013

The 21 ALOS PALSAR-1 scenes acquired between October 2007 and January 2011 from tracks 124 and 125 were grouped to form short paired temporal baselines to reduce measurement errors (Osmanoglu et al., 2013b). However, due to acquisition gaps, especially over austral winter months, there are some pairs with longer baselines. Surface velocity time series can be constructed with an inversion similar to small baselines analysis (Berardino et al., 2002; Lanari et al., 2007). However, the poor velocity estimates for pairs with long temporal baselines do not allow for construction of a redundant network, where each scene is connected with more than one pair. Therefore, the velocity time series were constructed based on the measured displacements for each pair.

In addition to averaging data from multiple pairs to increase the coverage and statistical significance of the annual surface velocity field, we also investigate the temporal variations of the surface velocities at the flux gates, and analyse their seasonality and their impact on resulting frontal ablation estimates for all calculated flux-gates.

To analyse the temporal variations of surface velocities at the flux gates, we computed average detrended velocities at the given flux gates. We did not attempt to estimate trends in surface velocity, because our velocity measurement period is too short to estimate linear trends in velocity and, if any, these would likely be associated with the increase in velocity experienced as the glacier ice approaches the calving front, and thus not representing a change in velocity with time at a given spatial location (Eulerian velocity) but a change in velocity of a given particle with time (Lagrangian velocity). Velocities were computed for all available periods spanning 46 to 368 days. The magnitude of the temporal variations of surface velocities was approximated as the standard deviation of the computed velocities. The flux gate length, average ice thickness and standard deviation of detrended surface velocities were used to calculate 1σ contribution of temporal variations of velocity to the estimated ice flux.

Seasonal variations were modelled by fitting a periodic signal (cosine) to the weighted observations of detrended velocities. The inverse of temporal baselines were selected as weights such that the shortest possible temporal baseline (of 46 days) has

TCD
7, 4207–4240, 2013

a weight of 1, while longer baselines have proportionally lower weights. The periodic signal does not account for interannual variations, yet it provides a measure of the seasonal amplitude and timing over the study period.

4.4 Ice thickness

Ice thickness observations are not available for any of the flux-gates, except for Johnsons Glacier (19 in Fig. 2). Therefore, we estimate the ice thickness at the flux-gates from surface velocity field following the method proposed by Rignot (1996) for ocean-terminating glaciers and also applied on King George Island by Osmanoglu et al. (2013a):

$$u_{\mathrm{sfc}} = (1-f)\left(\left[\frac{\tau_{\mathrm{d}}}{B}\right]^{n} E\widehat{H}\right) + f\left(\frac{\tau_{\mathrm{d}}}{R}\right)^{m} \quad (4)$$

$$\tau_{\mathrm{d}} = \rho_{\mathrm{ice}} g \widehat{H} \sin\alpha \quad (5)$$

where u_{sfc} is the surface velocity obtained from intensity feature tracking, f is an adjustable parameter between 0 and 1 setting the amount of sliding ($f = 0$, no sliding; $f = 1$, free sliding), n is the Glen's flow law parameter, τ_{d} is the gravitational driving stress, B is the column-averaged stiffness parameter in Glen's flow law, E is the flow law enhancement factor, $\widehat{H}$ is the estimated ice thickness, R is a constant including the effects of bed roughness, and m is the Weertman's sliding law parameter. In Eq. (5), g is gravity, and α is the surface slope. The deformation component of Eq. (4) assumes deformation by simple shear, i.e. it does not include the effect of longitudinal stress gradients. In contrast to Rignot (1996), we treat E as an adjustable parameter rather than a constant. Typical values for E are in the range 0.5 – 10, however values outside this range have also been reported (Greve and Blatter, 2009). For this analysis we calculate B based on ice temperature defined by an Arrhenius relationship (–3 °C, $B = 231\,866\,\mathrm{kPa\,a^{-1/3}}$), while we set R as $4\,\mathrm{kPa\,m^{-1/2}\,a^{-1/2}}$ (Rignot, 1996; Greve and Blatter, 2009; Cuffey and Paterson, 2010). The m and n parameters are set to 2 and

TCD
7, 4207–4240, 2013

3 respectively, while a truncated-Newton iterative optimization routine is used to find f and E using the available thickness data (Fig. 2).

In order to improve the fit we separated the surface velocity fields into slow (0–50 m yr^{-1}), medium (50–100 m yr^{-1}) and fast (>100 m yr^{-1}) moving glacier regions, and fitted Eq. (4) for each region separately.

4.5 Error analysis

The analysis carried out in this study introduces errors at various steps: (1) derived surface velocities from intensity offset tracking of PALSAR-1 images, (2) conversion of surface velocity to thickness-averaged velocity, (3) inference of ice thickness from thickness-averaged velocity and surface slope, including assumptions of the physical model and of the model parameter values, and (4) selection of flux gates. All error sources, except the latter, can be quantified by comparing the estimated ice thickness with available data. Errors in this paper are calculated from the difference between the observed and estimated ice thickness (Fig. 4), where 95 % of the data is covered inside the dashed lines defined with the minimum β angle (30°). There is a root mean square (rms) misfit of 103.44 m between the estimated and observed thickness data, indicating a poor fit.

5 Results

5.1 Surface velocities

Average surface ice velocities obtained from SAR intensity offset tracking are shown in Fig. 5a. Spatially incoherent velocity measurements are masked out, and appear as white. According to our results, Huron Glacier (7) has the fastest flowing ice, with velocities up to 250 m yr^{-1}. Kaliakra (6), Perunika (21) and Charity (17) glaciers also show large surface velocities. Unfortunately, for none of these areas are there in-situ ice surface measurements against which to compare our remotely-sensed velocities.

TCD
7, 4207–4240, 2013

The temporal variations in ice velocities for each flux-gate are shown in Fig. 6. The data show large temporal variability. The seasonality of these variations is approximated by fits to the periodic curves. Although the scatter is large and the data density limited, velocities generally tend to be higher during summer than winter as also indicated in some cases by a relatively high correlation coefficient. However, in other cases the fits are rather poor or even meaningless, indicating that the velocity variations do not follow a simple seasonal pattern, or the data density insufficient, or there are uncertainties too large to infer seasonal patterns. To explore a possible correlation of the velocity variations with air temperature, the figure also marks the periods of continuous daily mean temperatures above 0 °C.

5.2 Ice thickness

The ice thickness estimated from the average surface velocities (Fig. 5a) and the combined DEM (Fig. 3) using Eqs. (4) and (5) is shown in Fig. 5b. The computed ice thickness values are in the same range as the GPR measurements, however the fit between the estimated and measured data sets indicates large errors (Fig. 4).

5.3 Frontal ablation

Frontal ablation rates for all investigated tidewater glaciers are given in Table 1. The largest rate is found for Huron Glacier (7, Fig. 2), followed by glacier basin 3. Ice discharge for all glaciers totals $509 \pm 381\,\mathrm{Mt\,yr^{-1}}$. This is equivalent to a specific mass change of $-0.8 \pm 0.6\,\mathrm{m\,w.e.\,yr^{-1}}$ over the total area of the analysed basins ($599\,\mathrm{km^2}$) and $-0.7 \pm 0.5\,\mathrm{m\,w.e.\,yr^{-1}}$ over the area of the whole ice cap ($697\,\mathrm{km^2}$).

The changes in frontal ablation ΔD_{seas} for each basin, associated with the seasonal variations in surface velocity described earlier and characterised by their standard deviation σ_{vel}, are given in Table 1. The largest variation in frontal ablation occurs at basin 3 and is $42.9\,\mathrm{Mt\,yr^{-1}}$. In terms of specific units, the discharge variations attain their highest value of $1.0\,\mathrm{m\,w.e.\,yr^{-1}}$ at basin 10. The total variation of frontal ablation from

TCD
7, 4207–4240, 2013

all basins reaches 237 Mt yr^{-1}, which is less than the total uncertainty estimated for the frontal ablation (381 Mt yr^{-1}) but is still a matter of concern, as it is 46 % of the best estimate for the frontal ablation (509 Mt yr^{-1}).

6 Discussion

6.1 Frontal ablation

The only available detailed estimate of calving losses on Livingston ice cap is that of Johnsons Glacier (19 in Fig. 2). Using a full-stokes dynamical model constrained by measured velocities near the calving front, Navarro et al. (2013) calculated calving losses of 0.74 ± 0.17 Mt yr^{-1} averaged over the period May 2004–August 2007. This estimate compares reasonably well with our estimated value of 0.4 ± 0.3 Mt yr^{-1} for the period 2008–2011 (Table 1).

Our ice cap-wide frontal ablation estimate for Livingston Island is consistent with the results from a similar study on neighboring King George Island. Osmanoglu et al. (2013a) estimated that King George Island (1127 km^2) lost 720 ± 428 Mt yr^{-1} during the period October 2007–January 2011. The corresponding specific rate of 0.6 ± 0.4 m w.e. yr^{-1} is similar to Livingston's rate of 0.7 ± 0.5 m w.e. yr^{-1}. The lower relative error of the estimate for King George Island is mostly due to wider coverage of GPR ice thickness observations. On Livingston Island many of the available ice thickness measurements, mostly close to the ice divides in the western part of the ice cap, could not be used for the tuning of model parameters because ice velocities could not be derived from SAR data in these areas.

Our ice cap-wide frontal ablation estimate is in the range of the ice discharge estimates for individual glaciers after collapse of the Larsen-B and respective dynamic adjustments, Evans Glacier (459 Mt yr^{-1}, 2008) or Jorum Glacier main branch (534 Mt yr^{-1}, 2008) (Rott et al., 2011), though the specific rates for these glaciers (2.19 and 1.68 m w.e. yr^{-1}, respectively) are 2–3 times larger than that of Livingston Island.

TCD
7, 4207–4240, 2013

Except for Columbia Glacier in Alaska (O'Neel et al., 2005) estimates in specific units are considerably higher for King George Island and Livingston Island ice caps than those reported from glaciers in the Arctic (AMAP, 2011).

6.2 Uncertainties

The large discrepancies between the calculated and observed thicknesses shown in Fig. 4 (rms misfit of 103.4 m) indicate that our estimates of frontal ablation for Livingston Island should be considered only as a rough first-order approximation. The large errors result from a combination of those inherent to the estimation of surface velocities from PALSAR-1 images, those intervening in the conversion of surface velocity to thickness-averaged velocity using Eq. (2), and those involved in the retrieval of ice thickness from thickness-averaged velocity and surface slope using Eqs. (4) and (5). In our case, the latter are expected to be dominant. This error component encompasses both the limitations of the physical model and the choice of values for the model parameters.

The physical model represented by Eqs. (4) and (5) assumes deformation by simple shear, neglecting longitudinal stress gradients which are known to be important near the calving fronts because of the large values of the along-flow gradient of the surface velocity. Consequently, the ice thickness inferred near the calving fronts, where the ice fluxes are computed, are expected to be poor, implying large errors in the ice discharge calculation. Using a single fit of the parameters E and f all over the Livingston ice cap, as done in Osmanoglu et al. (2013a) for the neighboring King George Island ice cap, resulted in large errors (rms misfits >200 m). Using separate fits for the regions of slow, medium and fast flow, as described in Sect. 5.2, allowed us to significantly reduce the error, though the current rms misfit (103.4 m) is still very large.

Another limitation is the assumption of steady-state in Eqs. (4) and (5). The assumption is necessary to infer an ice-thickness distribution from velocity and surface slope data alone, without available thinning rate data. On Livingston Island, glacier thinning has only been studied on the Hurd Peninsula (Ximenis et al., 1999; Molina et al., 2007) (Fig. 2). Combined with observed front retreat on most of the ice cap (Calvet et al.,

TCD
7, 4207–4240, 2013

1999) this suggests that the current geometry of the ice cap is not stationary. Even if the surface mass balance data for the last decade on Hurd Peninsula is rather close to zero, indicating a deceleration of the mass losses as compared to previous decades (Navarro et al., 2013), the surface geometry needs some time to accommodate to the changing mass budget. This, however, occurs faster in tidewater glaciers as compared to land-terminating glaciers, because the former have larger velocities.

6.3 Temporal variations in surface velocities and associated changes in frontal ablation

Noticeable temporal variations in surface velocities at the given flux gates are apparent from both Fig. 6 and the σ_{vel} values in Table 1. However, these variations do not always exhibit a clear seasonality, as shown by the large scatter of values of the coefficients of determination r^2 given in Fig. 6. Clear seasonal variations in surface velocity are observed for several basins on Livingston Island. In particular, basins 6 (Kaliakra), 9 and 10 show large amplitudes and r^2 values above 0.55. Since these measurements are averaged along ten parallel flux gates for each basin and for every image-pair used in this analysis, it is very unlikely that these variations could arise from an error in our analysis. Fig. 6 also illustrates that the velocities tend to be higher during summer than winter ($29.7 \pm 17.3\,m\,yr^{-1}$ for summer vs. $19.7 \pm 12.2\,m\,yr^{-1}$ for winter), which suggests that high velocities in Livingston Island glaciers could often correspond to periods of strong melting at the glacier surface and associated changes in the water supply to the glacier bed, with corresponding changes in basal water pressure (e.g. Sugiyama et al., 2011). However, high velocities are sometimes observed during winter time. Occasional periods of surface melting and liquid precipitation events during the winter are not unusual in this region, which could imply basal water pressure changes and associated speed-up events during the winter time.

Regardless of the underlying mechanism for the temporal variations in surface velocity, these can exert a relatively strong influence on the frontal ablation rates, as shown in Table 1. The group of basins to the northern and north-eastern parts of the island

TCD
7, 4207–4240, 2013

(1–6), most of them having large frontal ablation rates, shows a consistently large value for the frontal ablation change associated with seasonal variations of velocity as compared to the frontal ablation estimated for each basin. The large value of the sum of frontal ablation changes for all the analysed basins, which is equivalent to 46 % of the frontal ablation for the whole Livingston Island, stresses the importance of the strong effect that the period of measurement can have on the estimates of frontal ablation.

6.4 Relative contribution of frontal ablation to total ablation

For Johnsons Glacier, using Navarro et al. (2013) data it can be estimated that, over the period April 2006–March 2008, the losses by frontal ablation represent only 16 % of the total annual ablation, the remaining originating from surface ablation (assuming basal melting and internal accumulation were negligible). However, this glacier has a very particular setting, with a very shallow pro-glacial bay (just a few meters depth), a nearly flat bed in the area close to the calving front and moderate frontal velocities (maximum values of the order of 40 m yr^{-1}), implying a small flux of ice into the ocean. Aside from some observations on Rotch Dome (westernmost part of the ice cap) during 1971–1974 (Orheim and Govorukha., 1982), the surface mass balance of the ice cap has only been studied on Hurd Peninsula (Ximenis et al., 1999; Navarro et al., 2013). The latter study includes mass balance profiles (summer, winter and annual) averaged over the period 2002–2011 for Johnsons (tidewater, 5.36 km^2) and Hurd (land-terminating, 4.03 km^2) glaciers.

To compare the frontal ablation rates to mass change due to surface processes we perform a simple back-of-the-envelope calculation and approximate ice cap-wide annual surface mass balance and total ablation rates. Based on surface mass balance observations on land-terminating Hurd and marine-terminating Johnsons glaciers we determine linear summer balance gradients by regressing summer surface balances averaged over 20 m altitude bands vs. altitude for the mass-balance years 2008–2011 (approximately overlapping with the time span of our velocity measurements; unpublished data from Francisco Navarro) and apply them to the hypsometry of our new

TCD
7, 4207–4240, 2013

DEM. Hence, we assume the gradient to be valid for the entire ice cap (Fig. 7). We apply Johnsons Glacier's gradient to all tidewater basins (96.8 % of total area), and Hurd Glacier's gradient to all land-terminating basins (3.2 %). For elevations where the gradient yields positive summer balances we assume 0 m w.e. yr^{-1}.

We use the same approach for computing glacier-wide winter balances but we assume that above 600 m a.s.l. the winter balance remains constant. Altitudes above 600 m correspond to mountain areas (mostly to the Friesland Massif, reaching 1700 m) which occupy a limited planar area of ~ 6.3 % of the ice cap. As a sensitivity test we also computed the winter balance where the gradient of winter surface mass balance vs. elevation was applied for the entire elevation range. We found no significant difference in results between both methods.

The gradient method yielded mean glacier-wide summer balance and winter balance of -0.7 ± 0.0 m w.e. yr^{-1} and 0.8 ± 0.1 m w.e. yr^{-1}, respectively. The resulting mean annual surface mass balance for the entire Livingston Island is 0.1 ± 0.1 m w.e. yr^{-1}, which, added to the contribution to mass balance by frontal ablation (-0.7 ± 0.5) gives a total mass balance for Livingston Island of -0.6 ± 0.5 m w.e. yr^{-1}.

To quantify the partitioning of total annual ablation we equate summer balance with total annual surface ablation, thus assuming summer snow accumulation to be negligible. We find that frontal ablation and surface ablation contribute equal shares to the total annual ablation of Livingston Island. This contribution of frontal ablation to the total ablation is even larger than that of Arctic ice caps such as the Academy of Sciences Ice Cap, in Severnaya Zemlya (Dowdeswell et al., 2002), and Austonna, in Svalbard (Dowdeswell et al., 2008), which show contributions of frontal ablation to the total ablation of 30–40 %.

7 Conclusions

Major outlet glaciers on Livingston Island are discharging a total of 509 ± 381 Mt yr^{-1}, which is equivalent to a specific mass change of -0.7 ± 0.5 m w.e. yr^{-1} calculated over

TCD
7, 4207–4240, 2013

the entire ice-covered area of 697 km^2, and is coincident with a rough estimate of the surface ablation during the period analysed. Therefore, frontal ablation and surface ablation contribute equal shares to total ablation of Livingston Island. Uncertainties in ice thickness estimation hinder the accuracy of the obtained results, so future work should focus on improving the ice thickness estimates across flux-gates.

Considerable temporal variations in ice velocity at the analysed flux gates are observed, with associated changes in frontal ablation for the entire Livingston Island of $\sim 237\,Mt\,yr^{-1}$, which is 46 % of the estimated frontal ablation. This stresses the importance of taking into account the temporal variations in ice velocity when computing frontal ablation with a flux-gate approach. The velocity variations do not always show a clear seasonality. Velocities tend to be higher during the summer, though occasionally high values are also observed during the winter. This suggests that changes in basal water pressure, associated with either strong surface melting or rainfall events (which sometimes occur during the winter), are likely the main drivers of the temporal variations in surface velocity, but further studies are needed to explore the causes of the observed temporal variations in ice velocities.

Acknowledgements. Funding was provided by NSF project #ANT-1043649, NASA project #NNX11A023G, DFG #BR2105/9-1 and the National Plan of R&D (Spain) project CTM2011-28980. We thank the ESF ERANET Europolar IMCOAST project (BMBF award AZ 03F0617B), EU FP7-PEOPLE-2012-IRSES IMCONet grant 318718, and Alaska Satellite Facility for data provision.

References

AMAP: Snow, Water Ice and Permafrost in the Arctic (SWIPA): Climate Change and the Cryosphere, vol. xii, Arctic Monitoring and Assesment Programme (AMAP), Oslo, Norway, 2011. 4222

Amundson, J. M. and Truffer, M.: A unifying framework for iceberg-calving models, J. Glaciol., 56, 822–830, 2010. 4209

TCD
7, 4207–4240, 2013

Balik, F., Alkis, A., Kurucu, Y., and Alkis, Z.: Validation of radargrammetric dem generation from radarsat images in high relief areas in Edremit region of Turkey, in: XXth ISPRS Congress Technical Commission II, vol. XXXV, Istanbul, Turkey, 150–155, 2004. 4214

Balz, T., He, X., Zhang, L., and Liao, M.: TerraSAR-X stereo radargrammetry for precise DEM generation in South-East Asia, in: Proceedings of Asian Conference on Remote Sensing, 2009. 4214

Balz, T., Zhang, L., and Liao, M.: Direct stereo radargrammetric processing using massively parallel processing, ISPRS J. Photogramm. Remote Sens., 79, 137–146, 2013. 4214

Bamber, J. and Gomez-Dans, J. L.: The accuracy of digital elevation models of the Antarctic continent, Earth Planet. Sc. Lett., 237, 516–523, 2005. 4215

Bassis, J. N.: The statistical physics of iceberg calving and the emergence of universal calving laws, J. Glaciol., 57, 3–16, 2011. 4209

Benn, D. I., Hulton, N. R., and Mottram, R. H.: "Calving laws", "sliding laws" and the stability of tidewater glaciers, Ann. Glaciol., 46, 123–130, 2007a. 4209

Benn, D. I., Warren, C. R., and Mottram, R. H.: Calving processes and the dynamics of calving glaciers, Earth-Sci. Rev., 82, 143–179, 2007b. 4209

Berardino, P., Fornaro, G., Lanari, R., and Sansosti, E.: A new algorithm for surface deformation monitoring based on small baseline differential SAR Interferograms, IEEE Geosci. Remote S., 40, 2375–2383, doi:10.1109/TGRS.2002.803792, 2002. 4217

Bliss, A., Hock, R., and Cogley, J.: A new inventory of mountain glaciers and ice caps for the Antarctic periphery, Ann. Glaciol., 54, 191–199, 2013. 4208, 4235

Calvet, J., García Sellés, D., and Corbera, J.: Fluctuaciones de la extensión del casquete glacial de la isla Livingston (Shetland del Sur) desde 1956 hasta 1996, Acta geológica hispánica, 34, 365–374, 1999. 4210, 4222

Chen, C. W. and Zebker, H. A.: Two-dimensional phase unwrapping with use of statistical models for cost functions in nonlinear optimization, J. Opt. Soc. Am. A, 18, available at: http://josaa.osa.org/abstract.cfm?URI=josaa-18-2-338, 338–351, 2001. 4214

Cogley, J.: The future of the world's glaciers, in: The Future of the World's Climate, 197–222, 2012. 4209

Cogley, J. G., Hock, R., Rasmussen, L. A., Arendt, A. A., Bauder, A., Braithwaite, R. J., Jansson, P., Kaser, G., Möller, M., Nicholson, L., and Zemp, M.: Glossary of Glacier Mass Balance and Related Terms, 2011. 4209

TCD
7, 4207–4240, 2013

Cuffey, K. and Paterson, W.: The Physics of Glaciers, Glacier Depth Average Velocity, Academic Press 2010. 4216, 4218
DOS: British Antarctic Territory, South Shetland Islands, Sheet W 62 60, Scale 1 : 200 000, D.O.S. 610 (Series D501), Pub. Directorate of Overseas Surveys, 1968. 4212
Dowdeswell, J. A., Bassford, R. P., Gorman, M. R., Williams, M., Glazovsky, A. F., Macheret, Y. Y., Shepherd, A. P., Vasilenko, Y. V., Savatyuguin, L. M., Hubberten, H.-W., and Miller, H.: Form and flow of the Academy of Sciences Ice Cap, Severnaya Zemlya, Russian High Arctic, J. Geophys. Res., 107, 2076, doi:10.1029/2000JB000129, 2002. 4208, 4225
Dowdeswell, J., Benham, T., Strozzi, T., and Hagen, J.: Iceberg calving flux and mass balance of the Austfonna ice cap on Nordaustlandet, Svalbard, J. Geophys. Res.-Earth, 113, F03022, doi:10.1029/2007JF000905, 2008. 4208, 4225
Eineder, M.: Efficient simulation of SAR Interferograms of large areas and of rugged terrain, IEEE Geosci. Remote S., 41, 1415–1427, 2003. 4213
Enderlin, E. M. and Howat, I. M.: Submarine melt rate estimates for floating termini of Greenland outlet glaciers (2000–2010), J. Glaciol., 59, 67–75, 2013. 4209
Giesen, R. H. and Oerlemans, J.: Climate-model induced differences in the 21st century global and regional glacier contributions to sea-level rise, Clim. Dynam., 40, 7–8, 2013. 4209
Gonzalez, J. H., Bachmann, M., Krieger, G., and Fiedler, H.: Development of the TanDEM-X calibration concept: analysis of systematic errors, IEEE Geosci. Remote S., 48, 716–726, 2010. 4214
Gray, A., Mattar, K., Vachon, P., Bindschadler, R., Jezek, K., Forster, R., and Crawford, J.: InSAR results from the RADARSAT Antarctic Mapping Mission data: estimation of glacier motion using a simple registration procedure, in: Geoscience and Remote Sensing Symposium Proceedings, 1998, IGARSS'98, 1998 IEEE International, vol. 3, 1638–1640, 1998. 4216
Greve, R. and Blatter, H.: Dynamics of Ice Sheets and Glaciers, Springer Verlag„ 2009. 4218
Hengl, T. and Reuter, H.: How accurate and usable is GDEM?, a statistical assessment of GDEM using LiDAR data, Geomorphometry, 2, 45–48, 2011. 4214
Hirt, C., Filmer, M., and Featherstone, W.: Comparison and validation of recent freely-available Aster-Gdem Ver1, SRTM Ver4. 1 And Geodata DEM-9S Ver3 Digital Elevation Models Over Australia, Aus. J. Earth Sci., 57, 337–347, 2010. 4214
Jonsell, U. Y., Navarro, F. J., Bañón, M., Lapazaran, J. J., and Otero, J.: Sensitivity of a distributed temperature-radiation index melt model based on AWS observations and surface en-

TCD
7, 4207–4240, 2013

ergy balance fluxes, Hurd Peninsula glaciers, Livingston Island, Antarctica, The Cryosphere, 6, 539–552, doi:10.5194/tc-6-539-2012, 2012. 4210
Lanari, R., Casu, F., Manzo, M., Zeni, G., Berardino, P., Manunta, M., and Pepe, A.: An overview of the small baseline subset algorithm: a DInSAR technique for surface deformation analysis, Pure Appl. Geophys., 164, 637–661, 2007. 4217
Liu, H., K. J.: Radarsat Antarctic Mapping Project digital elevation model version 2. Boulder, CO: National Snow and Ice Data Center, Digital media, available at: http://nsidc.org/data/nsidc-0082.html, 2001. 4213
Macheret, Y., Otero, J., Navarro, F., Vasilenko, E., Corcuera, M., Cuadrado, M., and Glazovsky, A.: Ice thickness, internal structure and subglacial topography of Bowles Plateau ice cap and the main ice divides of Livingston Island, Antarctica, by ground-based radio-echo sounding, Ann. Glaciol., 50, 49–56, 2009. 4211
Magruder, L. A., Webb, C. E., Urban, T. J., Silverberg, E. C., and Schutz, B. E.: ICESat altimetry data product verification at white sands space harbor, IEEE Geosci. Remote S., 45, 147–155, 2007. 4214
Marzeion, B., Jarosch, A. H., and Hofer, M.: Past and future sea-level change from the surface mass balance of glaciers, The Cryosphere, 6, 1295–1322, doi:10.5194/tc-6-1295-2012, 2012. 4209
Molina, C., Navarro, F., Calvet, J., Garcia-Selles, D., and Lapazaran, J.: Hurd Peninsula glaciers, Livingston Island, Antarctica, as indicators of regional warming: ice-volume changes during the period 1956–2000, Ann. Glaciol., 46, 43–49, 2007. 4211, 4222
Motyka, R. J., Hunter, L., Echelmeyer, K. A., and Connor, C.: Submarine melting at the terminus of a temperate tidewater glacier, LeConte Glacier, Alaska, USA, Ann. Glaciol., 36, 57–65, 2003. 4209
Navarro, F., Otero, J., Macheret, Y., Vasilenko, E., Lapazaran, J., Ahlstrom, A., and Machio, F.: Radioglaciological studies on Hurd Peninsula glaciers, Livingston Island, Antarctica, Ann. Glaciol., 50, 17–24, 2009. 4211
Navarro, F., Jonsell, U., Corcuera, M., and Martín-Español, A.: Decelerated mass loss of Hurd and Johnsons glaciers, Livingston Island, Antarctic Peninsula, J. Glaciol., 59, 115–128, 2013. 4209, 4210, 4221, 4223, 4224
O'Neel, S., Pfeffer, W., Krimmel, R., and Meier, M.: Evolving force balance at Columbia Glacier, Alaska, during its rapid retreat, J. Geophys. Res, 110, F03012, doi:10.1029/2005JF000292, 2005. 4222

TCD
7, 4207–4240, 2013

Orheim, O. and Govorukha., L.: Present-day glaciation in the South Shetland Islands, Ann. Glaciol., 3, 233–238, 1982. 4224

Osmanoglu, B., Dixon, T. H., Wdowinski, S., and Cabral-Cano, E.: On the importance of Path for Phase Unwrapping in Synthetic Aperture Radar Interferometry, Appl. Optics, 50, 3205–3220, doi:10.1364/AO.50.003205, available at: http://www.opticsinfobase.org/ao/abstract.cfm?uri=ao-50-19-3205, 2011. 4216

Osmanoglu, B., Braun, M., Hock, R., and Navarro, F.: Surface velocity and ice discharge of the ice cap on King George Island, Antarctica, Ann. Glaciol., 54, 111–119, 2013a. 4209, 4216, 4218, 4221, 4222

Osmanoglu, B., Dixon, T., and Wdowinski, S.: 3-D phase unwrapping for satellite radar interferometry, I: DEM generation, in press, 2013b. 4217

Otero, J.: Generación automática de malla de elementos finitos en modelos evolutivos de dinámica de glaciares, Ph.D. thesis, Universidad Politécnica de Madrid, ETSI de Caminos, Canales y Puertos, 2008. 4210, 4211

Otero, J., Navarro, F., Martin, C., Cuadrado, M., and Corcuera, M.: A three-dimensional calving model: numerical experiments on Johnsons Glacier, Livingston Island, Antarctica, J. Glaciol., 56, 200–214, 2010. 4209, 4210, 4211

Radić, V. and Hock, R.: Regionally differentiated contribution of mountain glaciers and ice caps to future sea-level rise, Nat. Geosci., 4, 91–94, 2011. 4209

Radić, V., Bliss, A., Beedlow, A. C., Hock, R., Miles, E., and Cogley, J. G.: Regional and global projections of twenty-first century glacier mass changes in response to climate scenarios from global climate models, Clim. Dynam., 22 pp., 2013. 4209

Reuter, H., Nelson, A., Strobl, P., Mehl, W., and Jarvis, A.: A first assessment of Aster Gdem Tiles for absolute accuracy, relative accuracy and terrain parameters, in: Geoscience and Remote Sensing Symposium, 2009 IEEE International, IGARSS 2009, vol. 5, V–240, 2009. 4214

Rignot, E.: Mapping of glacial motion and surface topography of Hielo Patagonico Norte, Chile, using satellite SAR L-band interferometry data, Ann. Glaciol., 23, 209–216, 1996. 4216, 4218

Rott, H., Müller, F., Nagler, T., and Floricioiu, D.: The imbalance of glaciers after disintegration of Larsen-B ice shelf, Antarctic Peninsula, The Cryosphere, 5, 125–134, doi:10.5194/tc-5-125-2011, 2011. 4221

TCD
7, 4207–4240, 2013

SGE: Spanish Antarctic Cartography, Livingston and Deception Islands, scale 1 : 100 000, 1st edn. Pub. Servicio Geográfico del Ejército, 1997. 4212

Shepherd, A. Ivins, E. R., A, G., Barletta, V. R., Bentley, M. J., Bettadpur, S., Briggs, K. H., Bromwich, D. H., Forsberg, R., Galin, N., Horwath, M., Jacobs, S., Joughin, I., King, M. A. Lenaerts, J. T. M., Li, J., Ligtenberg, S. R. M., Luckman, A., Luthcke, S. B., McMillan, M., Meister, R., Milne, G., Mouginot, J., Muir, A., Nicolas, J. P., Paden, J., Payne, A. J., Pritchard, H., Rignot, E., Rott, H., Sandberg Sørensen, L., Scambos, T. A., Scheuchl, B., Schrama, E. J. O., Smith, B., Sundal, A. V., van Angelen, J. H., van de Berg, W. J., van den Broeke, M. R., Vaughan, D. G., Velicogna, I., Wahr, J., Whitehouse, P. L., Wingham, D. J., Yi, D., Young, D., and Zwally, H. J.: A reconciled estimate of ice-sheet mass balance, Science, 338, 1183–1189, 2012. 4208

Steig, E. J. and Orsi, A. J.: Climate science: the heat is on in Antarctica, Nat. Geosci., 6, 87–88, 2013. 4209

Strozzi, T., Luckman, A., Murray, T., Wegmuller, U., and Werner, C.: Glacier motion estimation using SAR offset-tracking procedures, IEEE Geosci. Remote S., 40, 2384–2391, 2002. 4216

Strozzi, T., Kouraev, A., Wiesmann, A., Wegmüller, U., Sharov, A., and Werner, C.: Estimation of Arctic glacier motion with satellite L-band SAR data, Remote Sens. Environ., 112, 636–645, 2008. 4216

Sugiyama, S., Skvarca, P., Naito, N., Enomoto, H., Tsutaki, S., Tone, K., Marinsek, S., and Aniya, M.: Ice speed of a calving glacier modulated by small fluctuations in basal water pressure, Nat. Geosci., 4, 597–600, 2011. 4223

Truffer, M. and Fahnestock, M.: Rethinking ice sheet time scales, Science, 315, 1508–1510, 2007. 4209

Turner, J., Barrand, N. E., Bracegirdle, T. J., Convey, P., Hodgson, D. A., Jarvis, M., Jenkins, A., Marshall, G., Meredith, M. P., Roscoe, H., Shanklin, J., French, J., Goosse, H., Guglielmin, M., Gutt, J., Jacobs, S., Kennicutt, M. C. I., Masson-Delmotte, V., Mayewski, P., Navarro, F., Robinson, S., Scambos, T., Sparrow, M., Summerhayes, C., Speer, K., and Klepikov, A.: Antarctic climate change and the environment: an update, Polar Rec., 1–23, doi:10.1017/S0032247413000296, available at: http://journals.cambridge.org/article_S0032247413000296, 2013. 4209

Vieli, A. and Nick, F. M.: Understanding and modelling rapid dynamic changes of tidewater outlet glaciers: issues and implications, Surv. Geophys., 32, 437–458, 2011. 4209

TCD
7, 4207–4240, 2013

Werner, C., Wegmuller, U., Strozzi, T., and Wiesmann, A.: Precision estimation of local offsets between pairs of SAR SLCs and detected SAR images, in: Geoscience and Remote Sensing Symposium, 2005, IGARSS'05, Proceedings, 2005 IEEE International, vol. 7, 4803–4805, 2005. 4216

Ximenis, L., Calvet, J., Enrique, J., Corbera, J., Fernández de Gamboa, C., and Furdada i Bellavista, G.: The measurement of ice velocity, mass balance and thinning-rate on Johnsons Glacier, Livingston Island, South Shetland Islands, Antarctica, Acta geológica hispánica, 34, 406–409, 1999. 4210, 4211, 4222, 4224

TCD
7, 4207–4240, 2013

Table 1. Estimated frontal ablation rates for the period between October 2007 and January 2011, basin area, and average thickness and length of the flux-gates of all investigated tidewater glaciers on Livingston Island. σ_{vel} are the standard deviations of the computed temporal variations in velocities averaged over the flux gates and ΔD_{seas} are their associated changes in frontal ablation. Frontal ablation rates are given in Mt yr^{-1} and in specific units (m w.e. yr^{-1}).

Basin	Frontal ablation			Area		Avg. thick.	Length	σ_{vel}	ΔD_{seas}	
	Mt yr^{-1}	m w.e. yr^{-1}	%	km^{-2}	%	m	km	m yr^{-1}	Mt yr^{-1}	m w.e. yr^{-1}
1	42.7 ± 31.3	0.61 ± 0.45	8.4	69.6	11.6	180.3	16.8	10.2	25	0.4
2	5.3 ± 3.9	0.80 ± 0.59	1	6.7	1.1	126.6	3.7	7.8	3	0.4
3	69.8 ± 51.2	0.85 ± 0.62	13.7	82.1	13.7	172.2	22.7	13.5	42.9	0.5
4	58.8 ± 43.2	0.86 ± 0.63	11.6	68.3	11.4	152.5	18.1	11	24.6	0.4
5	18.8 ± 13.8	0.93 ± 0.68	3.7	20.3	3.4	153.8	7.7	16.5	15.9	0.8
6 (Kaliakra)	53.1 ± 39	0.83 ± 0.61	10.4	64.3	10.7	166.7	10.6	20.8	29.7	0.5
7 (Huron)	145.4 ± 114.1	2.69 ± 2.11	28.6	54.1	9	100.4	7.2	19.2	11.2	0.2
8	0.7 ± 0.5	0.15 ± 0.11	0.1	4.4	0.7	64.8	2.1	15.4	1.7	0.4
9	1.3 ± 0.9	0.74 ± 0.54	0.3	1.7	0.3	64.5	1.2	17.1	1.1	0.6
10	4.8 ± 3.5	0.90 ± 0.66	0.9	5.3	0.9	120.7	3.8	14.9	5.5	1.0
11 (Strandzha)	1.8 ± 1.3	0.82 ± 0.60	0.3	2.2	0.4	54.1	2.1	14.3	1.3	0.6
12 (Dobrudzha)	4.1 ± 3	0.48 ± 0.35	0.8	8.7	1.5	84.8	2.8	19.6	3.8	0.4
13 (Magura)	0.4 ± 0.3	0.37 ± 0.28	0.1	1.1	0.2	52.4	1	14	0.6	0.6
14 (Srebarna)	4.8 ± 3.5	1.07 ± 0.78	0.9	4.4	0.7	74.2	2.3	22.7	3.1	0.7
15 (Macy)	2.4 ± 1.8	0.08 ± 0.06	0.5	30.1	5	70.6	3.4	17.2	3.4	0.1
16 (Prespa)	8.7 ± 6.4	0.68 ± 0.50	1.7	12.7	2.1	81.9	3.5	23.3	5.4	0.4
17 (Charity)	1.0 ± 0.7	0.15 ± 0.11	0.2	6.6	1.1	95.2	3.1	14.5	3.4	0.5
18 (Huntress)	15.2 ± 11.2	0.37 ± 0.27	3	40.8	6.8	108.1	4.3	15	5.7	0.1
19 (Johnsons)	0.4 ± 0.3	0.07 ± 0.05	0.1	5.3	0.9	120.5	2.1	8.7	1.8	0.3
20	2.6 ± 1.9	0.20 ± 0.15	0.5	13.2	2.2	141.4	3	10.9	3.8	0.3
21 (Perunika)	23.8 ± 17.5	0.71 ± 0.52	4.7	33.7	5.6	168.9	6.2	18	15.3	0.5
22	10.0 ± 7.3	1.21 ± 0.89	2	8.3	1.4	131.9	5	9.3	4.9	0.6
23	6.9 ± 5.1	0.58 ± 0.43	1.4	11.8	2	120.1	4.8	10.5	4.9	0.4
24	26.1 ± 19.2	0.60 ± 0.44	5.1	43.7	7.3	152.2	13.8	11	18.8	0.4
Total	508.9 ± 381.0	0.85 ± 0.64	100	599.4	100				236.8	0.4
Entire ice cap		0.73 ± 0.55		697.3						0.3

TCD
7, 4207–4240, 2013

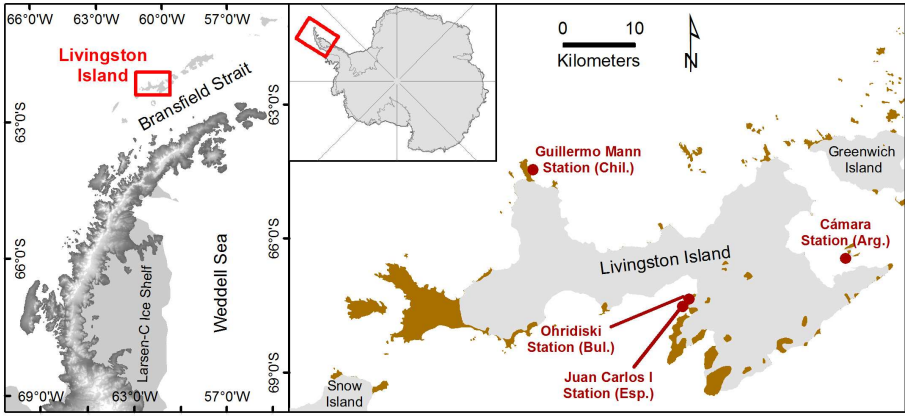

Fig. 1. Location of Livingston Island, to the northwest of the tip of the Antarctic Peninsula. Green colour denotes ice-free areas, while grey is used for glaciated areas. Note that in subsequent figures only the glaciated area of the island is shown. Map base: SCAR Antarctic Digital Database, Vers. 6.0; MOA coastline of Antarctica, NSIDC.

TCD
7, 4207–4240, 2013

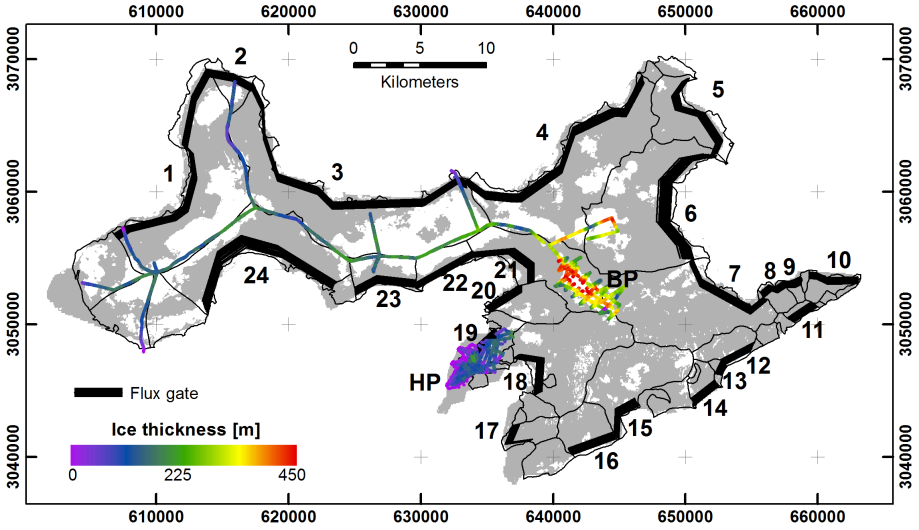

Fig. 2. Livingston Island glacier basins, according to Bliss et al. (2013). Numbers indicate the basins analysed in this study. Grey shading marks the area for which ice velocities could be derived from SAR data. Thick black lines denote flux gates used for computing ice discharge. Ice thicknesses obtained from GPR measurements are shown in color. HP denotes Hurd Peninsula, and BP Bowles Plateau.

TCD
7, 4207–4240, 2013

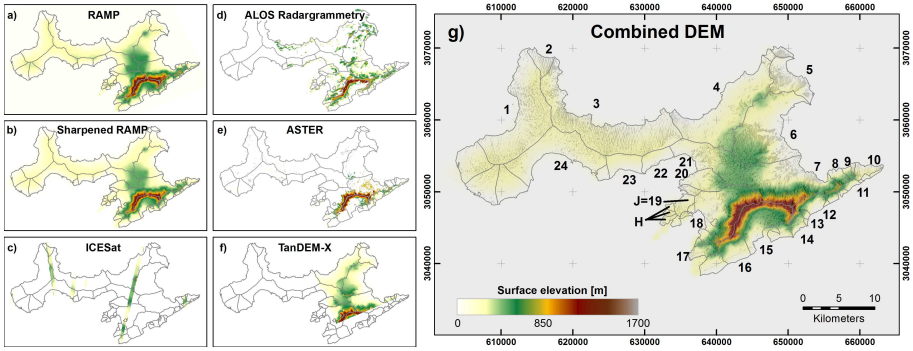

Fig. 3. Digital elevation data used in this analysis. There are 792 ICESat data points distributed among five different satellite tracks. Radargrammetry and ASTER data provide elevations outside the TanDEM-X coverage. Hurd Glacier and Johnsons Glacier, where surface mass balance observations are available, are labelled by H and J, respectively.

TCD
7, 4207–4240, 2013

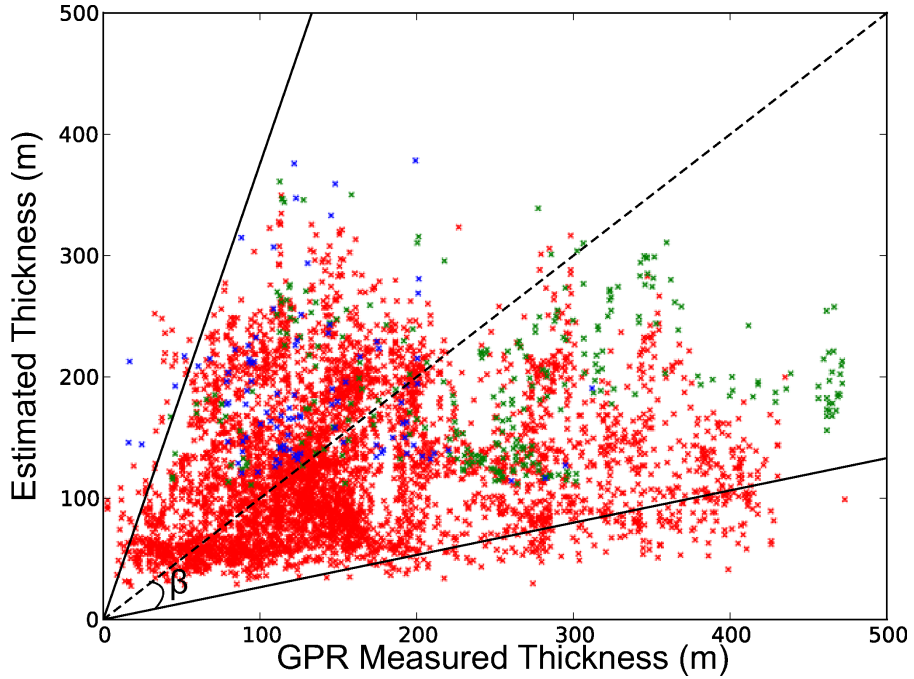

Fig. 4. Measured vs. estimated ice thickness according to Eq. (4). The dashed line indicates the 1-to-1 line. Continuous lines show the 95 % error boundary corresponding to $\beta = 30^{\circ}$. Red, green and blue colours are used to distinguish points from the slow, medium and fast moving glacier regions, respectively.

TCD
7, 4207–4240, 2013

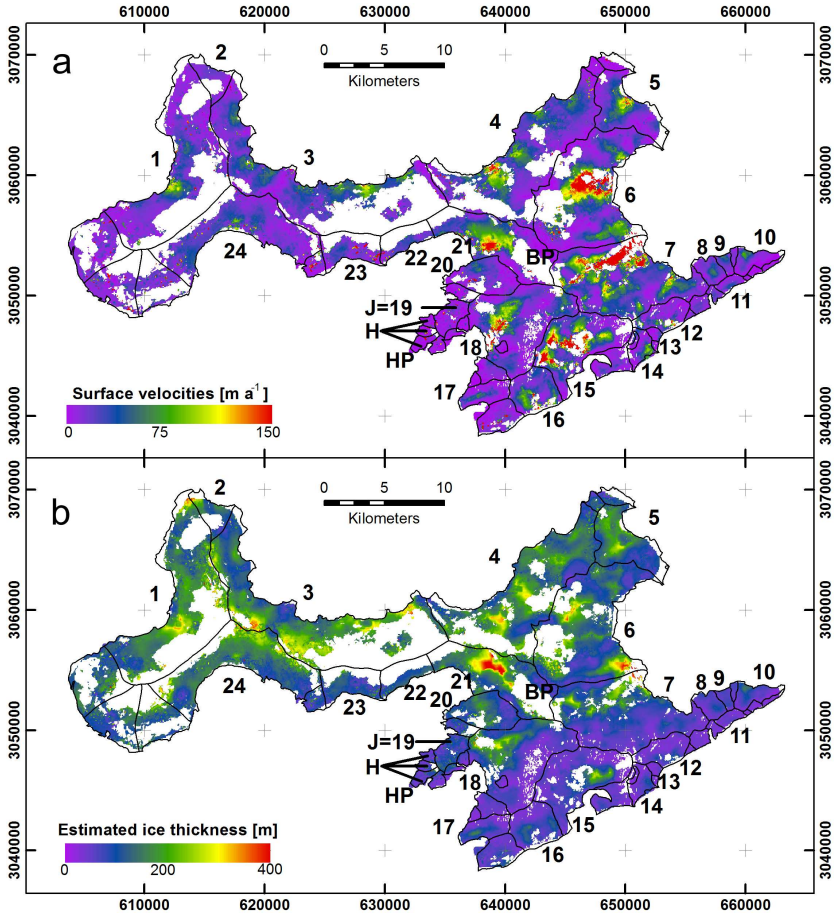

Fig. 5. (a) Surface velocities obtained from SAR feature tracking. Huron Glacier (7) shows the fastest flow. **(b)** Estimated ice thickness computed from surface velocity using Eq. (4).

TCD
7, 4207–4240, 2013

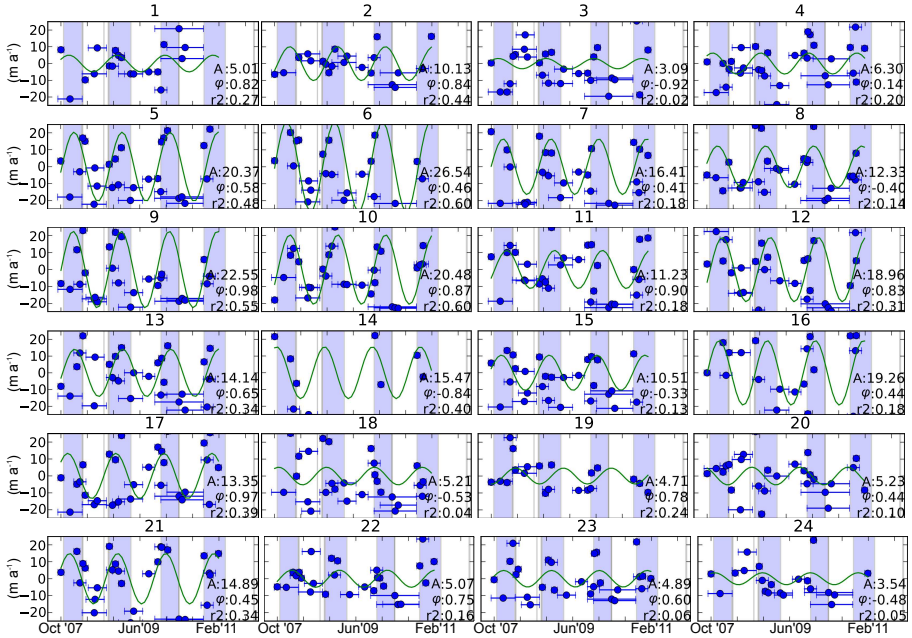

Fig. 6. Detrended velocity time series for all analysed tidewater glaciers. Velocities are averaged over each glacier's flux gate and shown as deviations of each glacier's mean over the period October 2007–January 2011. Fits to a periodic signal and their amplitude A, phase ϕ and r^2 value are shown to illustrate the seasonality. Larger amplitudes indicate stronger seasonal effects, and phase values are reported in partial years. Continuous periods with daily air temperature exceeding 0 °C are shaded in blue, using the temperature records from Juan Carlos I weather station (12 m a.s.l.). Horizontal bars indicate the time interval of each measurement (temporal baseline).

TCD
7, 4207–4240, 2013

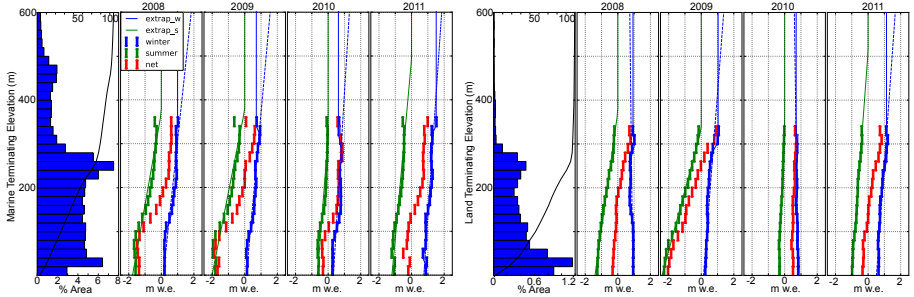

Fig. 7. Surface mass balance estimates extrapolated from Johnsons and Hurd Glaciers to the hypsometry of the whole ice cap for different years. Cumulative distributions of total area for each glacier type are shown as the black solid line, with a second x-axis shown on the upper border. The green and blue lines show extrapolated summer and winter balances. For winter balances the dashed lines indicate constant gradient approach, while the solid line indicates constant final value approach. Summer balances use the constant gradient approach with a cut-off at zero.

TCD
7, 4207–4240, 2013